Journal of Materials Chemistry C

PAPER

View Article Online
View Journal | View Issue

Cite this: J. Mater. Chem. C, 2018, 6, 6216

Photophysics behind highly luminescent two-dimensional hybrid perovskite $(CH_3(CH_2)_2NH_3)_2(CH_3NH_3)_2Pb_3Br_{10}$ thin films†

Daniel Ramirez, *[a] José Ignacio Uribe, [ab] Luca Francaviglia, [c] Pablo Romero-Gomez,[c] Anna Fontcuberta i Morral [c] and Franklin Jaramillo *[a]

Received 5th April 2018,
Accepted 10th May 2018

DOI: 10.1039/c8tc01582a

rsc.li/materials-c

Two-dimensional (2D) Ruddlesden–Popper perovskites have emerged as a new class of hybrid materials with high photoluminescence and improved stability compared to their three-dimensional (3D) counterparts. Studies of the photophysics of these new 2D perovskites are essential for the fast development of optoelectronic devices. Here, we study the power and temperature dependences of the photoluminescence properties of the $(PA)_2(MA)_2Pb_3Br_{10}$ hybrid perovskite. High electron–phonon coupling near room temperature was found to be dominated by longitudinal optical (LO) phonons *via* the Fröhlich interaction. However, we show that the presence of free carriers is also possible, with lower trapping states and higher and more stable emission compared to the 3D $MAPbBr_3$. These characteristics make the studied 2D material very attractive for optoelectronic applications, including solar cells and light emitting diodes (LEDs). Our investigation provides new fundamental insights into the emission characteristics of 2D lead halide perovskites.

Introduction

Three dimensional (3D) hybrid metal halide perovskites (ABX_3) have demonstrated outstanding optoelectronic properties and thus have been applied with success in the areas of solar cells[1–3] and light emitting diodes.[4,5] Among them, the ability to modulate the emission peak in the visible range by changing the halide (X = Cl, Br or I) in $CH_3NH_3PbX_3$[6] and $CsPbX_3$[7] has opened new avenues for LEDs. As an example, an emission peak around 540 nm is obtained when X = Br.[8] The reported exciton binding energy for this kind of perovskite is comparable to the thermal energy at room temperature (RT).[9,10] As a consequence, excitons will tend to dissociate into free carriers (FCs) rather than recombine radiatively. In addition, 3D perovskite structures have demonstrated stability issues, which challenges their future commercialization.

Two-dimensional (2D) Ruddlesden–Popper perovskites have recently emerged as a new class of quantum-well (QW) like materials with improved stability and astounding high photoluminescence (PL). Recent work reports PL with a quantum yield (PLQY) close to 35%, which can be increased to 80% with a surface passivation treatment.[11] 2D perovskites are described by the formula $A_2A_{n-1}'B_nX_{3n+1}$ where A, A′ are cations, B is a metal and X is a halide; with the *n*-value determining the QW thickness[12] and, as a result, the degree of quantum and dielectric confinement as well as the optical band gap.[13] The optoelectronic properties can be tuned by modifying the chemical composition and quantum confinement. More importantly, 2D perovskites offer a reduced ion migration, which renders them environmentally stable. Thus, 2D perovskites turn out to be more attractive than their 3D counterparts in many applications.[14–16] Still, some fundamental aspects such as charge-carrier dynamics and emission characteristics are unexplored. This fundamental understanding is necessary before the optoelectronic properties of devices can be further improved.[17]

In this work, we synthesized and investigated the photophysical properties of a new 2D Ruddlesden–Popper hybrid perovskite with the formula $(CH_3(CH_2)_2NH_3)_2$ $(CH_3NH_3)_2Pb_3Br_{10}$, simplified as $(PA)_2(MA)_2Pb_3Br_{10}$. We used $CH_3NH_3PbBr_3$ ($MAPbBr_3$) as a 3D reference material for comparison. Our power and temperature dependent photoluminescence measurements indicate that $(PA)_2(MA)_2Pb_3Br_{10}$ exhibits homogeneous and stable emission from 10 to 350 K. Compared to the 3D perovskite counterpart, it exhibits a higher PLQY and lower charge-carrier trapping, demonstrating the potential of this material for optoelectronic applications.

[a] Centro de Investigación, Innovación y Desarrollo de Materiales – CIDEMAT, Facultad de Ingeniería, Universidad de Antioquia UdeA, Calle 70 No. 52-21, Medellín, Colombia. E-mail: estiben.ramirez@udea.edu.co, franklin.jaramillo@udea.edu.co
[b] Grupo de Estado Sólido, Instituto de Física, Universidad de Antioquia UdeA, Calle 70 No. 52-21, Medellín, Colombia
[c] Laboratoire des Matériaux Semiconducteurs, Institut des Matériaux, Ecole Polytechnique Fédérale de Lausanne, 1015 Lausanne, Switzerland

† Electronic supplementary information (ESI) available: AFM and KPFM image of the 2D perovskite. Temperature dependent PL spectra. Explanatory note for the temperature dependent PL analysis. See DOI: 10.1039/c8tc01582a

Experimental

Materials and synthesis

Methylammonium bromide (MABr) and propylammonium bromide (PABr) from Dyesol were used as organic cations. Dimethyl sulfoxide (DMSO, Sigma Aldrich) and dimethylformamide (DMF, Alfa Aesar) were used as solvents, and lead bromide ($PbBr_2$) (Alfa Aesar) as a lead source. In order to obtain the $MAPbBr_3$ precursor solution, MABr and $PbBr_2$ were dissolved in DMSO (1 : 1 : 1 molar ratio; 50% wt.) and *N*,*N*-dimethylformamide (DMF, Alfa Aesar). The precursor solution of the layered perovskites was obtained in a similar way. The concentration was 45% wt and the molar ratio was $MABr : PABr : PbBr_2$ (2 : 2 : 3). The films were obtained by spin coating the precursor solutions on top of a glass substrate at 4000 rpm for 25 s. The films were then annealed at 65 °C for 1 min plus 100 °C for 10 min.

Characterization

X-ray diffractograms were collected from $2\theta = 5^\circ$ to 50° in a Bragg–Brentano geometry from the prepared thin films with a PANalytical diffractometer, using Cu Kα (1.5408 Å) radiation with a step size of 0.04° and a speed of 2° per minute. Optical absorption was measured in the range of 300–850 nm using a Cary 100 spectrometer. AFM, topographic 2 × 2 μm measurements were performed with a MFP-3D AFM (Asylum Research), data were taken using tapping mode, and the tips used were Pt coated silicon with a nominal spring constant of 2.89 N m^{-1} and a resonance frequency of 75 KHz. For the measurement of the electrode work function (WF), the tip was calibrated using a gold surface (WF = 5.1 eV). Power and temperature photoluminescence measurements were performed using a single-frequency optically-pumped semiconductor laser as a continuous-wave excitation source with a wavelength at 488 nm. The laser power was controlled by ND filters and monitored by a power meter placed after a 50 : 50 beam splitter. The second path in the beam splitter sent the laser light through an objective (NA = 0.75) that focused the laser on the sample into a spot of about 1 μm in diameter. The luminescence light was collected through the same objective and sent to a 500 mm spectrometer where a 600 l mm^{-1} grating was used to separate the signal from the laser reflection and disperse it onto a multichannel charged-coupled-device (CCD). For the measurements performed at different temperatures, the sample was placed on the cold finger of a helium cryostat. The temperature was controlled by a built-in resistive heater with negative feedback with respect to the chosen temperature setpoint.

Photoluminescence quantum yield (PLQY) calculation

PLQY measurements were acquired following the protocol described by de Mello *et al.*[18] using an integrating sphere setup. A 480 nm laser (Coherent, Sapphire 488–100 CW SF CDRH) was used to excite the samples and neutral density filters were used to attenuate the laser intensity.

Results and discussion

Both $MAPbBr_3$ and $(PA)_2(MA)_2Pb_3Br_{10}$ were deposited by spin coating on glass substrates and the characterization measurements were achieved in the solid state. Fig. 1a shows X-ray diffraction measurements of the two materials, along with the theoretical predictions. Highly oriented cubic $MAPbBr_3$ was confirmed by the existence of the (100) and (200) diffraction peaks at 15.05° and 30.27°.[8] Similarly, the experimental diffractogram for $(PA)_2(MA)_2Pb_3Br_{10}$ indicated a high orientation in the (202) plane, in good agreement with the already reported structure.[19] In Fig. 1b we depict the layered structure of the $(PA)_2(MA)_2Pb_3Br_{10}$, in which MA^+ molecules are located inside the $\langle PbBr_6^{2-} \rangle$ octahedrons and separated by the PA^+ layers. Fig. 1c shows the surface morphology of the $(PA)_2(MA)_2Pb_3Br_{10}$ film studied by atomic force microscopy (AFM). The measurements reveal well-defined crystalline domains with sizes ranging from 0.5 μm to 1.0 μm. In addition to AFM, we also performed Kelvin probe force microscopy (KPFM) maps (see ESI,† Fig. S1). We obtained a work function of 5.23 ± 0.05 eV, which would facilitate the injection of holes from a p-type semiconductor such as PEDOT:PSS in LED applications.[20]

Fig. 2a shows the absorption spectra of $MAPbBr_3$ and $(PA)_2(MA)_2Pb_3Br_{10}$. The absorption spectrum of the 3D $MAPbBr_3$ is characterized by an excitonic peak at the onset of absorption around 525 nm, as previously reported for 3D perovskites.[21] $(PA)_2(MA)_2Pb_3Br_{10}$ showed a less well-defined onset absorption, with the highest absorption in the 450–475 nm range. The calculated band gap from the Tauc plots (Fig. S2, ESI†) resulted to be 2.31 eV and 2.36 eV for the 3D and the 2D perovskite, respectively.

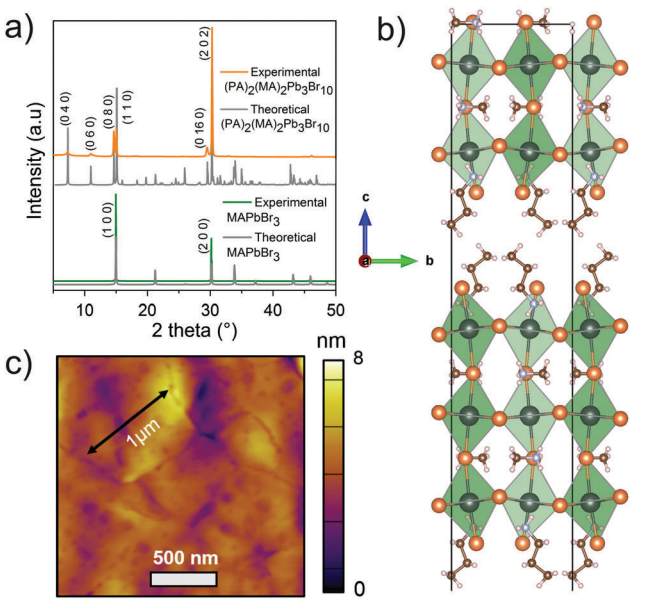

Fig. 1 (a) X-ray diffractogram for $MAPbBr_3$ and $(PA)_2(MA)_2Pb_3Br_{10}$ thin films, (b) crystalline structure of $(PA)_2(MA)_2Pb_3Br_{10}$, where small gray dots correspond to nitrogen atoms, brown dots to carbon atoms, pink dots to hydrogen atoms, orange dots to bromine and large green dots to lead atoms. (c) Atomic force microscopy (AFM) topographic image of a thin film of $(PA)_2(MA)_2Pb_3Br_{10}$.

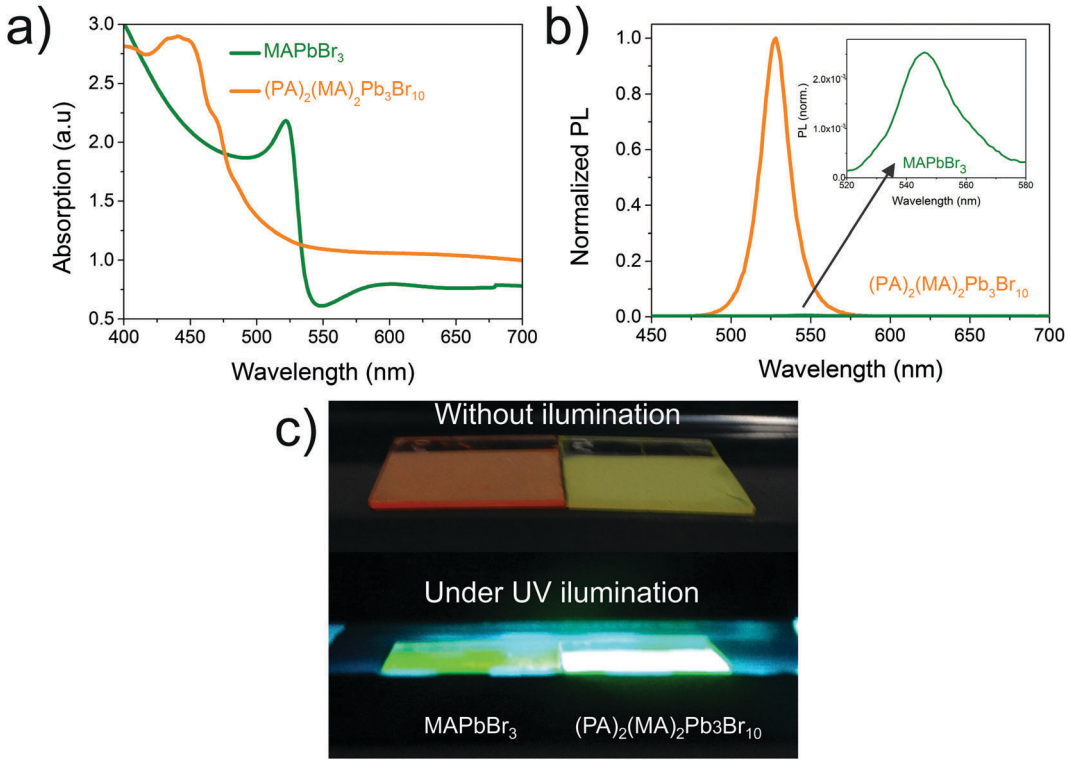

Fig. 2 (a) Absorption spectra of $MAPbBr_3$ and $(PA)_2(MA)_2Pb_3Br_{10}$ thin films, (b) room temperature PL spectrum of $(PA)_2(MA)_2Pb_3Br_{10}$ with an inset of $MAPbBr_3$ and (c) images of $MAPbBr_3$ and $(PA)_2(MA)_2Pb_3Br_{10}$ under UV illumination. Note that the absorption does not go to zero due to scattering of the surface roughness.

Fig. 2b compares the PL spectra of both samples excited at 450 nm. $(PA)_2(MA)_2Pb_3Br_{10}$ has a strong room-temperature PL, with a peak at 529 nm. The PL signal was three orders of magnitude higher than the $MAPbBr_3$ reference sample (inset of Fig. 2b). We also excited at a different wavelength and the result was the same (Fig. S3, ESI†). To make evident the higher emission of the 2D sample, Fig. 2c shows the comparative emission of the films when they are exposed to UV light. Even though the original films were different in color, orange in the case of the 3D and yellow for the 2D, they presented a green emission, in agreement with their emission peaks at 545 nm and 529 nm, respectively.

The low PL yield of the 3D perovskite is in agreement with the current understanding: even at room temperature, excitons are almost ionized into free carriers, and the non-radiative recombination due to a high density of trap states reduces the PL emission. In the case of quantum-confined systems one expects the photo-generated electrons and holes to be strongly bound by Coulomb interactions into excitons. Therefore, we believe quantum confinement can be responsible for the high PL yield of the 2D perovskite, as well as for the recently proved dissociation of excitons into longer-lived free-carriers through layer edge states (LES).[13] The high luminescence yield is an indirect indication of a reduced density of trap states inside the band gap.[22] This characteristic is essential to obtain a high open-circuit voltage, V_{oc}, in solar cells or high performance LEDs.

Light emission in semiconductors can involve exciton recombination, free-carrier recombination, free-to-bound recombination and donor–acceptor pair recombination.[23] In order to have a better understanding of the origin of the emission of the 2D perovskite, we measured the PL spectra under various excitation densities, including intensities close to the photovoltaic regime.[24] Fig. 3a and b show the PL spectra of the two samples for different excitation powers. The PL line shapes are almost identical in the whole range of excitation intensity, with an excellent power-law dependence on the excitation power for both 2D and 3D perovskites. In direct bandgap semiconductors and under non-resonant excitation conditions, the integrated PL intensity (I_{PL}) is a power-law function of the excitation density with $k = 2$ for free carrier (FC) recombination, $1 < k < 2$ for the recombination of excitons (including free excitons and bound excitons) and $k < 1$ for free-to-bound and donor–acceptor pair recombination.[25] The calculated k value for the 3D and 2D perovskite was 1.489 and 1.037, respectively (Fig. 3c). This value agrees well with reports on exciton radiative recombination in semiconductors.[26] Among other reasons, a higher density of crystal imperfections or a larger contribution of FC recombination accounts for the higher k value of the 3D perovskite. It is important to note that k values of $\sim$1.5 are commonly found in the 3D $CH_3NH_3PbI_3$ and $CH_3NH_3PbI_{3-x}Cl_x$ films, due to their lower binding energy and the coexistence of exciton and FC recombination at room temperature.[23] The lower value for

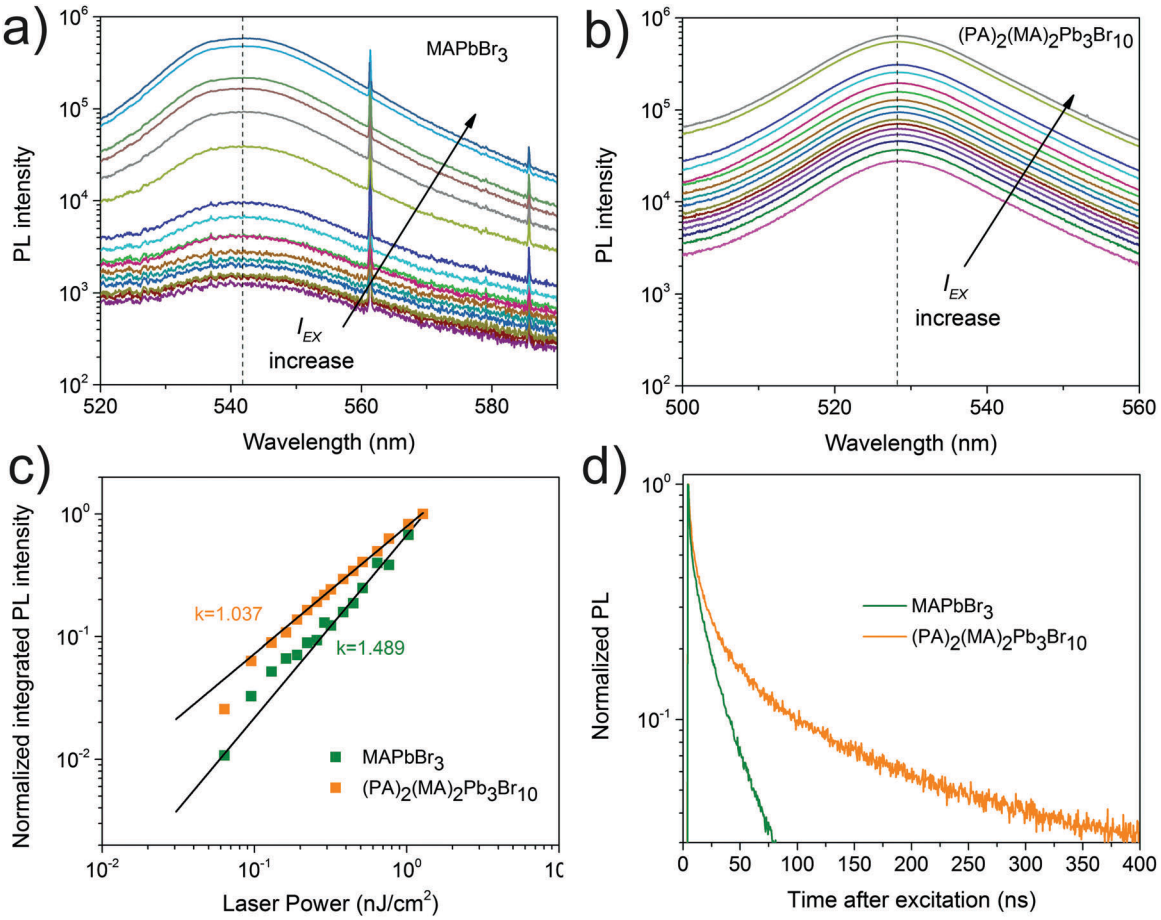

Fig. 3 PL spectra of (a) $MAPbBr_3$ and (b) $(PA)_2(MA)_2Pb_3Br_{10}$ thin films as a function of the excitation density from 0.05 to 2 nJ cm^{-2}, (c) Logarithmic plot of the integrated PL intensity *versus* excitation density and (d) time-resolved PL decay of $MAPbBr_3$ and $(PA)_2(MA)_2Pb_3Br_{10}$. Note that the narrow peaks in Fig. 3a are noisy due the proximity of the laser wavelength and the PL peak.

the 2D perovskite is in agreement with its predominant excitonic behavior due its higher quantum confinement.

As shown in Fig. 3d, different to the 3D perovskite, long-lived charges are found in the 2D material indicating that recombination is not dominated by non-radiative decay mechanisms such as reduced electron–phonon coupling[27] or electronic impurities.[28]

Comparative temperature-dependent PL spectra of both the 3D and 2D perovskites over the 10 to 350 K range are plotted in Fig. S4 (ESI†) and summarized in Fig. 4. The temperature-dependent PL for the 3D perovskite showed two main characteristics. The first one is the emission peak decay in intensity and its shift from higher wavelengths to lower wavelengths (blue shift) as temperature increases, as shown in Fig. 4a. The second one is the appearance of a second peak for temperatures below 140 K. This second peak at around 580 nm shows a very small shift in energy as function of temperature (Fig. S4a, ESI†). Note that the 2D sample showed a single PL peak in the entire temperature range.

The multiple peaks of the 3D perovskite are consistent with previous PL results of MA-containing perovskites. The observed inhomogeneous broadening and multi-peak emission at low temperatures is assigned to the coexistence of two perovskite phases (*i.e.* cubic and tetragonal).[29] Recently, Wright *et al.*[30] showed that this second peak does not appear in the PL spectra of the equivalent formamidinium (FA) perovskites. Therefore, we conclude that the second peak is not intrinsic to hybrid lead halide perovskites, but derives from trap states in the 3D perovskite. On the other hand, the single peak of the 2D perovskite exhibits a PLQY of 29.6% (similar to the value for 2D films without surface passivation)[11] compared to 3.5% for the 3D sample. This result suggests that the existence of trap states at low temperature is negligible and/or absent in the 2D perovskite, which is probably related to organic cations promoting 2D structures that can passivate grain boundaries, and therefore enhancing the PL yield.[31]

Fig. 4a shows that the 3D perovskite has a remarkable temperature-dependent blue shift of the PL peak position when the temperature is increased, whereas this shift for the 2D structure is less pronounced. Such a blue shift has been previously attributed to the thermal expansion of the lattice, consequently reducing the overlap between the Pb-6s and I-5p antibonding atomic orbitals forming the valence band maximum.[32] Therefore, the stabilization of the valence band maximum is less dependent in the 2D perovskite due to its larger lattice parameters, which results in a more stable electronic structure over the studied temperature range.

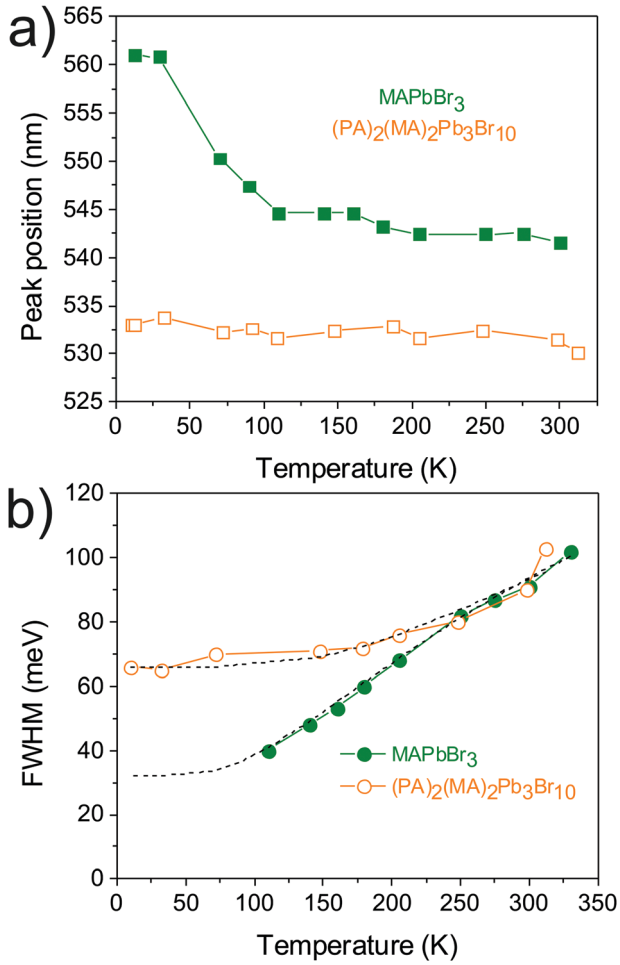

Fig. 4 Temperature dependence of the steady state (a) PL peak position and (b) FWHM for $MAPbBr_3$ and $(PA)_2(MA)_2Pb_3Br_{10}$. The dashed black line shows the fitting obtained by taking into account the temperature-independent inhomogeneous broadening Γ_0 and the interaction between charge carriers and longitudinal optical phonons (LO-phonons), as described by the Fröhlich Hamiltonian.

Fig. 4b shows the temperature dependence of emission broadening, a material feature commonly used to assess the mechanisms of electron–phonon coupling in a wide range of inorganic semiconductors, including hybrid perovskites. Such electron–phonon interactions matter, because they set a fundamental intrinsic limit to charge-carrier mobilities in the absence of extrinsic scattering of impurities or interfaces.[30] Additionally, electron–phonon coupling has been demonstrated to dominate homogeneous emission-line broadening in hybrid lead iodide perovskite at room temperature.[33] Different mechanisms of scattering between charge carriers and phonons or impurities are associated with different functional dependencies of the PL linewidth $\Gamma(T)$ on temperature. (See ESI† for a note on the detailed explanation of the studied model.) They can be combined in the following eqn (1):

$$\Gamma(T) = \Gamma_0 + \gamma_{LO}/e^{\left(\frac{E_{LO}}{k_B T}\right)} - 1 \quad (1)$$

Table 1 Extracted linewidth parameters

Sample	Γ_O/meV	γ_{LO}/meV	E_{LO}/meV
$MAPbBr_3$	32	190	29
$(PA)_2(MA)_2Pb_3Br_{10}$	66	230	55

Γ_0 is the temperature-independent inhomogeneous broadening term, which arises from scattering due to disorder and imperfections; γ_{LO} is the charge-carrier-phonon coupling strength for LO phonon (Fröhlich) scattering; E_{LO} is an energy of the weakly dispersive LO phonon branch; and k_B is the Boltzmann constant. The extracted fitted parameters from Fig. 4b are presented in Table 1.

Towards $T = 0$ K, $\Gamma(T)$ can be identified as the temperature-independent inhomogeneous broadening term Γ_0 arising from disorder. For $MAPbBr_3$ Γ_0 approaches 32 meV, which is in agreement with the similar value already reported in the literature.[30] On the other hand, Γ_0 for $(PA)_2(MA)_2Pb_3Br_{10}$ approaches a higher value of 66 meV. The values of γ_{LO} and E_{LO} were also higher for $(PA)_2(MA)_2Pb_3Br_{10}$, indicating that LO-phonon coupling in our 2D perovskite is higher than in the 3D one. However, it is not as high as in other 2D systems.[34] Therefore, this set of results combined with the previously demonstrated longer charge-carrier recombination lifetime and stable emission, allows us to deduce a contribution of FC recombination in the room temperature emission.

Conclusions

In conclusion, we showed the power and temperature dependent PL properties of both $MAPbBr_3$ and $(PA)_2(MA)_2Pb_3Br_{10}$ perovskites. We demonstrated that $(PA)_2(MA)_2Pb_3Br_{10}$ presents important figures of merit for optoelectronic and photovoltaic applications. Unlike the $MAPbBr_3$ perovskite, the $(PA)_2(MA)_2Pb_3Br_{10}$ exhibits a single emission peak in the temperature range from 10 K to 350 K, indicating the absence of excitonic trap states. Additionally, the 2D structure showed larger emission and a longer charge-carrier lifetime than its 3D counterpart. These observations suggest that FC recombination can also be present in this quantum-well like system. Finally, all of these aspects represent a great advantage and make $(PA)_2(MA)_2Pb_3Br_{10}$ a very promising material for applications in LEDs or solar cells.

Conflicts of interest

The authors declare that there are no conflicts of interest.

Acknowledgements

We thank the Colombian "Departamento Nacional de Planeaciòn", SGR collaborative project 2013000100184 between Empresas Públicas de Medellin, Andercol S. A., Sumicol S. A. S., and Universidad de Antioquia, for supporting this work. Authors from EPFL thank funding from H2020 through the Marie Curie Actions and the Swiss National Science Foundation *via* the NCCR QSIT.

References

1 D. Bi, W. Tress, M. I. Dar, P. Gao, J. Luo, C. Renevier, K. Schenk, A. Abate, F. Giordano, J.-P. Correa Baena, J.-D. Decoppet, S. M. Zakeeruddin, M. K. Nazeeruddin, M. Grätzel and A. Hagfeldt, *Sci. Adv.*, 2016, **2**, e1501170.
2 S. S. Mali, C. S. Shim and C. K. Hong, *NPG Asia Mater.*, 2015, **7**, e208.
3 N. Giesbrecht, J. Schlipf, L. Oesinghaus, A. Binek, T. Bein, P. Müller-Buschbaum and P. Docampo, *ACS Energy Lett.*, 2016, **1**, 150–154.
4 G. Li, Z.-K. Tan, D. Di, M. L. Lai, L. Jiang, J. H.-W. Lim, R. H. Friend and N. C. Greenham, *Nano Lett.*, 2015, **15**, 2640–2644.
5 G. Longo, A. Pertegás, L. Martínez-Sarti, M. Sessolo, H. J. Bolink, M. M. Lee, H. J. Snaith, A. Petrozza, F. D. Angelis, L. Manna, A. Petrozza, R. T. Phillips, R. H. Friend and R. H. Friend, *J. Mater. Chem. C*, 2015, **3**, 11286–11289.
6 Z. Xiao, R. A. Kerner, L. Zhao, N. L. Tran, K. M. Lee, T.-W. Koh, G. D. Scholes and B. P. Rand, *Nat. Photonics*, 2017, **11**, 108–115.
7 J.-H. Cha, J. H. Han, W. Yin, C. Park, Y. Park, T. K. Ahn, J. H. Cho and D.-Y. Jung, *J. Phys. Chem. Lett.*, 2017, **8**, 565–570.
8 X. Zhao, B. Zhang, R. Zhao, B. Yao, X. Liu, J. Liu and Z. Xie, *J. Phys. Chem. Lett.*, 2016, **7**, 4259–4266.
9 B. Wenger, P. K. Nayak, X. Wen, S. V. Kesava, N. K. Noel and H. J. Snaith, *Nat. Commun.*, 2017, **8**, 590.
10 A. Miyata, A. Mitioglu, P. Plochocka, O. Portugall, J. T. Wang, S. D. Stranks, H. J. Snaith and R. J. Nicholas, *Nat. Phys.*, 2015, **11**, 582–587.
11 M.-G. La-Placa, G. Longo, A. Babaei, L. Martínez-Sarti, M. Sessolo and H. J. Bolink, *Chem. Commun.*, 2017, **53**, 8707–8710.
12 D. B. Mitzi, *J. Chem. Soc., Dalton Trans.*, 2001, 1–12.
13 J.-C. Blancon, H. Tsai, W. Nie, C. C. Stoumpos, L. Pedesseau, C. Katan, M. Kepenekian, C. M. M. Soe, K. Appavoo, M. Y. Sfeir, S. Tretiak, P. M. Ajayan, M. G. Kanatzidis, J. Even, J. J. Crochet and A. D. Mohite, *Science*, 2017, **355**, 1288–1292.
14 J. Rodríguez-Romero, B. C. Hames, I. Mora-Sero and E. M. Barea, *ACS Energy Lett.*, 2017, **2**, 1969–1970.
15 Y. Lin, Y. Bai, Y. Fang, Q. Wang, Y. Deng and J. Huang, *ACS Energy Lett.*, 2017, **2**, 1571–1572.
16 J.-Y. Seo, J. Choi, H.-S. Kim, J. Kim, J.-M. Yang, C. Cuhadar, J. S. Han, S.-J. Kim, D. Lee, H. W. Jang and N.-G. Park, *Nanoscale*, 2017, **9**, 15278–15285.
17 R. K. Misra, B.-E. Cohen, L. Iagher and L. Etgar, *ChemSusChem*, 2017, **10**, 3712–3721.
18 J. C. De Mello, H. F. Wittmann and R. H. Friend, *Adv. Mater.*, 1997, **9**, 230–232.
19 D. Ramirez, Y. Suto, N. C. Rosero-Navarro, A. Miura, K. Tadanaga and F. Jaramillo, *Inorg. Chem.*, 2018, **57**, 4181–4188.
20 K. Qasim, B. Wang, Y. Zhang, P. Li, Y. Wang, S. Li, S.-T. Lee, L.-S. Liao, W. Lei and Q. Bao, *Adv. Funct. Mater.*, 2017, **27**, 1606874.
21 Y. Yang, Y. Yan, M. Yang, S. Choi, K. Zhu, J. M. Luther and M. C. Beard, *Nat. Commun.*, 2015, **6**, 7961.
22 T. Leijtens, G. E. Eperon, A. J. Barker, G. Grancini, W. Zhang, J. M. Ball, A. R. S. Kandada, H. J. Snaith and A. Petrozza, *Energy Environ. Sci.*, 2016, **9**, 3472–3481.
23 H. He, Q. Yu, H. Li, J. Li, J. Si, Y. Jin, N. Wang, J. Wang, J. He, X. Wang, Y. Zhang and Z. Ye, *Nat. Commun.*, 2016, **7**, 10896.
24 V. D'Innocenzo, G. Grancini, M. J. P. Alcocer, A. R. S. Kandada, S. D. Stranks, M. M. Lee, G. Lanzani, H. J. Snaith and A. Petrozza, *Nat. Commun.*, 2014, **5**, DOI: 10.1038/ncomms4586.
25 T. Schmidt, K. Lischka and W. Zulehner, *Phys. Rev. B: Condens. Matter Mater. Phys.*, 1992, **45**, 8989–8994.
26 H. Shibata, M. Sakai, A. Yamada, K. Matsubara, K. Sakurai, H. Tampo, S. Ishizuka, K.-K. Kim and S. Niki, *Jpn. J. Appl. Phys.*, 2005, **44**, 6113–6114.
27 Z. Guo, X. Wu, T. Zhu, X. Zhu and L. Huang, *ACS Nano*, 2016, **10**, 9992–9998.
28 X. Wu, M. T. Trinh, D. Niesner, H. Zhu, Z. Norman, J. S. Owen, O. Yaffe, B. J. Kudisch and X.-Y. Zhu, *J. Am. Chem. Soc.*, 2015, **137**, 2089–2096.
29 B. Tom, Y. Fang, J. M. Kadro, M. Schreyer, F. Wei, S. G. Mhaisalkar, M. Graetzel and T. J. White, *J. Mater. Chem. A*, 2013, **1**, 5628–5641.
30 A. D. Wright, C. Verdi, R. L. Milot, G. E. Eperon, M. A. Pérez-Osorio, H. J. Snaith, F. Giustino, M. B. Johnston and L. M. Herz, *Nat. Commun.*, 2016, **7**, DOI: 10.1038/ncomms11755.
31 D. S. Lee, J. S. Yun, J. Kim, A. M. Soufiani, S. Chen, Y. Cho, X. Deng, J. Seidel, S. Lim, S. Huang and A. W. Y. Ho-Baillie, *ACS Energy Lett.*, 2018, **3**, 647–654.
32 M. I. Dar, G. Jacopin, S. Meloni, A. Mattoni, N. Arora, A. Boziki, S. M. Zakeeruddin, U. Rothlisberger and M. Grätzel, *Sci. Adv.*, 2016, **2**, e1601156.
33 R. L. Milot, G. E. Eperon, H. J. Snaith, M. B. Johnston and L. M. Herz, *Adv. Funct. Mater.*, 2015, **25**, 6218–6227.
34 K. Thirumal, W. K. Chong, W. Xie, R. Ganguly, S. K. Muduli, M. Sherburne, M. Asta, S. Mhaisalkar, T. C. Sum, H. Sen Soo and N. Mathews, *Chem. Mater.*, 2017, **29**, 3947–3953.